

# Modified automatic term selection v2: A faster algorithm to calculate inelastic scattering cross-sections



Ján Rusz

Department of Physics and Astronomy, Uppsala University, P.O. Box 516, 75120 Uppsala, Sweden

## ARTICLE INFO

### Article history:

Received 12 November 2016

Revised 8 January 2017

Accepted 21 January 2017

Available online 25 January 2017

## ABSTRACT

We present a new algorithm for calculating inelastic scattering cross-section for fast electrons. Compared to the previous Modified Automatic Term Selection (MATS) algorithm (Rusz et al. [18]), it has far better convergence properties in zone axis calculations and it allows to identify contributions of individual atoms. One can think of it as a blend of MATS algorithm and a method described by Weickenmeier and Kohl [10].

© 2017 Elsevier B.V. All rights reserved.

Simulations of dynamical diffraction effects in elastic and inelastic scattering of electrons plays an important role in interpreting and predicting experimental observations and designing optimal measurement conditions.

For elastic scattering there exist two main classes of computational approaches, both in common use today: multislice (MS) method [1–3] and Bloch waves (BW) method [4,5]. Both have their strengths and weaknesses in specific situations. MS method is more versatile, capable to treat non-periodic systems, such as nano-structures or crystals with defects. Numerically it is a very efficient method, only dependent on the size of the structure model in question. BW method, on the other hand, is best suited to crystalline structures, for which it is very efficient, because it is independent of the thickness of the material. Its computational speed only depends on the number of atoms within a unit cell.

Treatment of inelastic scattering builds on these principles. BW method has been used since the works of Kainuma [6], explaining the formation of the Kikuchi patterns. The theory was further developed by Rossouw and Maslen [7], Kohl and Rose [8], Saldin [9], Weickenmeier and Kohl [10], and Nelhiebel et al. [11] among others.

The task is to evaluate the double-differential scattering cross-section (DDSCS)

$$\frac{\partial^2 \sigma}{\partial \Omega \partial E} \propto \sum_{\mathbf{a}} \sum_{\mathbf{g} \mathbf{h} \mathbf{g}'} \sum_{j l j' l'} X_{\mathbf{g} \mathbf{h} \mathbf{g}'}^{j l j' l'} e^{i(\mathbf{q}-\mathbf{q}') \cdot \mathbf{a}} \frac{S_{\mathbf{a}}(\mathbf{q}, \mathbf{q}', E)}{q^2 q'^2} \quad (1)$$

where

$$X_{\mathbf{g} \mathbf{h} \mathbf{g}'}^{j l j' l'} = C_{\mathbf{0}}^{(j)*} C_{\mathbf{g}}^{(j)} D_{\mathbf{0}}^{(l)} D_{\mathbf{h}}^{(l)*} e^{i \gamma^{(l)} t} \times C_{\mathbf{g}'}^{(j')} C_{\mathbf{g}}^{(j')*} D_{\mathbf{0}}^{(l')} D_{\mathbf{h}'}^{(l')*} e^{-i \gamma^{(l')} t} \quad (2)$$

$$\mathbf{q} = \mathbf{k}_f - \mathbf{k}_i + \mathbf{h} - \mathbf{g} + (\gamma^{(l)} - \gamma^{(j)}) \hat{\mathbf{n}}_z \quad (3)$$

$$\mathbf{q}' = \mathbf{k}_f - \mathbf{k}_i + \mathbf{h}' - \mathbf{g}' + (\gamma^{(l')} - \gamma^{(j')}) \hat{\mathbf{n}}_z. \quad (4)$$

In these equations,  $C_{\mathbf{g}}^{(j)}$  is so called Bloch coefficient corresponding to beam  $\mathbf{g}$  (a reciprocal lattice vector) and Bloch wave indexed by  $j$ . The  $C$ -coefficients describe incoming electron beam and  $D$ -coefficients describe outgoing electron beam – so called reciprocal wave determined by the detector orientation. Detector orientation also defines the outgoing wave-vector  $\mathbf{k}_f$  and experimental setup defines the incoming electron beam wavevector  $\mathbf{k}_i$ . Elongations of Bloch wave vectors are denoted  $\gamma^{(j)}$ ,  $\gamma^{(l)}$ , where  $j$ ,  $l$  index the incoming and outgoing Bloch waves, respectively. Further,  $t$  is the thickness of the sample and  $\mathbf{a}$  labels all the atom positions, on which an inelastic scattering event can occur. Finally,  $S_{\mathbf{a}}(\mathbf{q}, \mathbf{q}', E)$  is mixed dynamical form factor (MDFF, [8]) – the matrix element describing excitation of the sample by energy  $E$ , corresponding to momentum transfer vectors  $\mathbf{q}, \mathbf{q}'$ .

In parallel with these BW approaches, there is a whole class of MS-based methods for evaluation of the DDSCS. We refer the reader to a number of excellent articles about this approach, e.g., Refs. [12–15]. Here we will not describe these methods in further detail, because our focus will be on DDSCS summation in the reciprocal space. Alternative approaches include formulations based on density matrix; we again refer the reader to the original literature [16,17].

Returning to the BW methods, in Ref. [18] an efficient algorithm for calculation of such DDSCS has been described. There, the

E-mail address: [jan.rusz@fysik.uu.se](mailto:jan.rusz@fysik.uu.se)

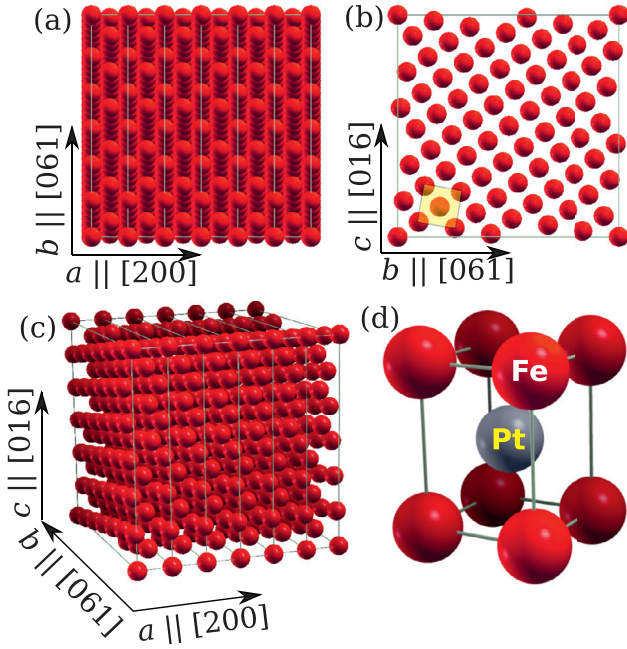


**Fig. 1.** Structure models used in test calculations. An orthogonal supercell of a body-centered cubic Fe crystal tilted in the three-beam orientation is depicted in (a) in top-view,  $ab$ -plane, (b) side-view,  $bc$ -plane, and (c) perspective view. The directions of supercell axes in terms of the Miller indices for a bcc-Fe unit cell are given in the figure. In panel (a) the supercell is repeated six times along the  $a$ -axis. A projection of single unit cell is overlaid in (b) in yellow color. (d) A perspective view of a primitive unit cell of FePt crystal. (For interpretation of the references to color in this figure legend, the reader is referred to the web version of this article.)

following approximation has been done to the MDFF term:

$$\frac{S_a(\mathbf{q}, \mathbf{q}', E)}{q^2 q'^2} \approx \frac{S_a(\tilde{\mathbf{q}}, \tilde{\mathbf{q}}', E)}{\tilde{q}^2 \tilde{q}'^2} \quad (5)$$

where

$$\tilde{\mathbf{q}} = \mathbf{k}_f - \mathbf{k}_i + \mathbf{h} - \mathbf{g} \quad (6)$$

$$\tilde{\mathbf{q}}' = \mathbf{k}_f - \mathbf{k}_i + \mathbf{h}' - \mathbf{g}', \quad (7)$$

i.e., assuming smallness of the BW vector elongations, compared to  $\mathbf{k}_f - \mathbf{k}_i$  or reciprocal lattice vectors. In the structure factor term  $e^{i(\mathbf{q}-\mathbf{q}') \cdot \mathbf{a}}$  the full  $\mathbf{q}, \mathbf{q}'$  momentum transfers, including Bloch wave elongations  $\gamma^{(j)}, \gamma^{(l)}$ , were naturally retained, otherwise there would be no thickness dependence of the resulting expression. Note that this does not mean that  $q_z$  was constant in the MDFF terms, because there are higher order Laue zones (HOLZ) typically included in the basis.

For the later convenience, we will here narrow down our description to a case of orthogonal unit cell with  $c$ -axis oriented parallel to the  $z$ -axis of the coordinate system. The beam entrance and exit surfaces will be assumed to be perpendicular to  $c$ -axis. If some other orientation of the crystal is desired, it is often possible to find an orthogonal structure model – a supercell – which fulfills these conditions. For example a cubic crystal with lattice constant  $a$ , oriented in systematic row condition with beam parallel to (016) direction, can be described by an orthogonal supercell with volume 37 times larger than the unit cell and with lattice parameters  $a \times \sqrt{37}a \times \sqrt{37}a$ , see Fig. 1(a)–(c).

Sum over atoms  $\mathbf{a}$  can be done in part analytically, since BW method is usually employed in cases with small periodically repeated unit cells. We can then write  $\mathbf{a} = \mathbf{R} + \mathbf{u}$ , where  $\mathbf{R}, \mathbf{u}$  are lattice and basis vectors, respectively. Lateral sum over lattice vectors

leads to a requirement that the in-plane component of  $\mathbf{q} - \mathbf{q}'$  must be a reciprocal lattice vector. Sum over the  $z$ -coordinate then gives a thickness-dependent function [19]

$$T_{jlj'l'}(t) = e^{i(\delta\gamma^{(jj')} + \delta\gamma^{(ll')}) \frac{t}{2}} \frac{\sin(\delta\gamma^{(jj')} - \delta\gamma^{(ll')}) \frac{t}{2}}{(\delta\gamma^{(jj')} - \delta\gamma^{(ll')}) \frac{t}{2}} \quad (8)$$

where for simplicity we have neglected absorption effects. The exponential factors from Eq. (2) were included into the thickness function.

This allows to cast the DDSCS into the following form:

$$\frac{\partial^2 \sigma}{\partial \Omega \partial E} = \sum_{\mathbf{ghg'h'}} \frac{1}{N_u} \sum_{\mathbf{u}} \frac{S_u(\tilde{\mathbf{q}}, \tilde{\mathbf{q}}', E)}{\tilde{q}^2 \tilde{q}'^2} e^{i(\tilde{\mathbf{q}} - \tilde{\mathbf{q}}') \cdot \mathbf{u}} \times \sum_{jlj'l'} Y_{\mathbf{ghg'h'}}^{jlj'l'} T_{jlj'l'}(t) \quad (9)$$

where

$$Y_{\mathbf{ghg'h'}}^{jlj'l'} = C_0^{(j)*} C_g^{(j)} D_0^{(l)} D_h^{(l)*} \times C_0^{(j')} C_g^{(j')} D_0^{(l')} D_h^{(l')*}. \quad (10)$$

The MATS algorithm introduced in the above-mentioned Ref. [18] then defines a cut-off parameter  $C_{\text{off}}$  and proceeds in the following way: One constructs lists of double products  $C_0^{(j)*} C_g^{(j)}$  and  $D_0^{(l)} D_h^{(l)*}$  with amplitude larger than cut-off, sorted by amplitude, and from them a list of quadruple products  $C_0^{(j)*} C_g^{(j)} D_0^{(l)} D_h^{(l)*}$  larger than cut-off and classified by  $\tilde{\mathbf{q}}$  and sorted by amplitude. Using this list one can efficiently evaluate the final sum, evaluating just one MDFF per pair of  $\tilde{\mathbf{q}}, \tilde{\mathbf{q}}'$ , i.e., fixed  $\mathbf{h} - \mathbf{g}$  and  $\mathbf{h}' - \mathbf{g}'$ , while summing over all  $j, l, j', l'$  terms larger than cut-off.

The MATS algorithm turned out to have very good convergence properties for plane-wave illumination case treated using purely Bloch waves methods [18,20]. Moreover, the computing time scales approximately inverse-proportionally to the cut-off parameter – a favorable scaling, considering that the DDSCS is expressed as an eight-fold summation over beams and Bloch-wave indices [18].

In a later extension for treatment of convergent electron beams with arbitrary aberrations or angular momentum [21], the elastic scattering of the incoming electron beam prior to the inelastic event has been treated by the MS method. A Fourier-transformed wavefunction of the scattered convergent beam can be mapped to Bloch coefficients and enter the same summation algorithm. While the overall shape of diffraction patterns showed typically a good convergence with respect to the cut-off parameter, in certain cases, often for the smallest scattering angles, the convergence was found to be rather slow (see below). The scaling of this combined MS/BW-MATS algorithm is slower with respect to cut-off, the computing time is approximately proportional to inverse square of the cut-off criterion and thus quickly becomes prohibitively slow, when an absolute convergence is needed.

This motivated us to develop a new algorithm, inspired by an earlier work of Weickenmeier and Kohl [10], where the DDSCS is expressed as a sum over atoms of a squared four-fold sum over beams and Bloch wave indices

$$\frac{\partial^2 \sigma}{\partial \Omega \partial E} \Big|_{if} \propto \sum_{\mathbf{a}} \left| \sum_{\mathbf{g}, \mathbf{h}} C_0^{(j)*} C_g^{(j)} D_0^{(l)} D_h^{(l)*} e^{i(\mathbf{q} \cdot \mathbf{a} - \gamma^{(l)} t)} S_{if}(\mathbf{q}) \right|^2 \quad (11)$$

here for simplicity given for a specific excitation from initial state  $|i\rangle$  to final state  $|f\rangle$  of a crystal

$$S_{if}(\mathbf{q}) = \langle f | \frac{e^{i\mathbf{q} \cdot \mathbf{r}}}{q^2} | i \rangle \quad (12)$$

A sum over available initial and final states yields the MDFF in the following way

$$\frac{S(\mathbf{q}, \mathbf{q}', E)}{q^2 q'^2} = \sum_{i, f} \langle i | \frac{e^{-i\mathbf{q}' \cdot \mathbf{r}}}{q'^2} | f \rangle \langle f | \frac{e^{i\mathbf{q} \cdot \mathbf{r}}}{q^2} | i \rangle \delta(E_i - E_f + E) \quad (13)$$

Although it is not strictly necessary, here we will consider dipole approximation for MDFF, in which it can be expressed as

$$S(\mathbf{q}, \mathbf{q}', E) = \mathbf{q} \cdot \mathbb{M}(E) \cdot \mathbf{q}' \quad (14)$$

where  $\mathbb{M}(E)$  is an energy-dependent  $3 \times 3$  Hermitean matrix. Since it is Hermitean, it is possible to diagonalize it, which then allows us to evaluate its square root. Here it will be useful to keep a careful matrix notation, therefore a real-valued bold-face vector  $\mathbf{q}$  will be understood as a column vector and then  $\mathbf{q}^T \equiv \mathbf{q}^\dagger$  will be the corresponding row vector. Diagonalizing the MDFF leads to (we temporarily drop the explicit marking of energy dependence)

$$S(\mathbf{q}, \mathbf{q}') = \mathbf{q}^T \mathbb{U} \mathbb{D} \mathbb{U}^\dagger \mathbf{q}' \quad (15)$$

where  $\mathbb{U}$  is a unitary matrix diagonalizing  $\mathbb{M}$  and  $\mathbb{D}$  are eigenvalues of  $\mathbb{M}$ , some of which can be negative. Taking a square root of the diagonal matrix leads to

$$S(\mathbf{q}, \mathbf{q}') = \mathbf{q}^T \mathbb{U} \mathbb{D}^{1/2} \mathbb{D}^{1/2} \mathbb{U}^\dagger \mathbf{q}' = [(\mathbb{D}^*)^{1/2} \mathbb{U}^\dagger \mathbf{q}]^\dagger (\mathbb{D}^{1/2} \mathbb{U}^\dagger \mathbf{q}') \quad (16)$$

This expression is already suitable for being introduced to the Eq. (11), where  $\frac{1}{q^2} \mathbb{D}^{1/2} \mathbb{U}^\dagger \mathbf{q}$  would formally replace  $S_{if}(\mathbf{q})$ . However, if we consider that in the dipole approximation matrices  $\mathbb{M}$ ,  $\mathbb{D}$ ,  $\mathbb{U}$  are independent of  $\mathbf{q}$ ,  $\mathbf{q}'$ , it is sufficient to calculate vectors

$$\mathbf{P}_{gh}^{jl} = C_0^{(j)*} C_g^{(j)} D_0^{(l)} D_h^{(l)*} e^{-i\gamma^{(l)} t} \frac{\mathbf{q}}{q^2} \quad (17)$$

for  $\mathbf{q}$ -vectors given as in Eqs. (3), (4) and for each atom we need to evaluate a sum resulting in vector

$$\mathbf{Q}(\mathbf{a}) = \sum_{g,j,h,l} \mathbf{P}_{gh}^{jl} e^{i\mathbf{q} \cdot \mathbf{a}} \quad (18)$$

The final DDSCS is then

$$\frac{\partial^2 \sigma}{\partial \Omega \partial E} \propto N(E) \sum_{\mathbf{a}} \mathbf{Q}(\mathbf{a})^\dagger \cdot \mathbb{M}(E) \cdot \mathbf{Q}(\mathbf{a}) \quad (19)$$

We illustrate this on two basic examples. First, for a non-magnetic cubic crystal one can write the MDFF as

$$S(\mathbf{q}, \mathbf{q}', E) = N(E) \mathbf{q} \cdot \mathbf{q}' \quad (20)$$

and the DDSCS becomes

$$\frac{\partial^2 \sigma}{\partial \Omega \partial E} \propto N(E) \sum_{\mathbf{a}} |\mathbf{Q}(\mathbf{a})|^2 \quad (21)$$

Second, if one is interested to calculate purely magnetic signal along the z-direction, MDFF can be calculated as

$$S(\mathbf{q}, \mathbf{q}', E) = iM(E)(\mathbf{q} \times \mathbf{q}')_z \quad (22)$$

leading to a simple expression

$$\left. \frac{\partial^2 \sigma}{\partial \Omega \partial E} \right|_{\text{mag}} \propto 2M(E) \sum_{\mathbf{a}} \text{Im}[Q_x^*(\mathbf{a}) Q_y(\mathbf{a})] \quad (23)$$

Similarly one can evaluate contributions to the DDSCS from all nine independent elements of a Hermitean  $3 \times 3$  matrix [22], to which one can uniquely decompose a general dipole approximation to MDFF.

Note that using  $\tilde{\mathbf{q}}$  instead of  $\mathbf{q}$  in the definition of  $\mathbf{P}_{gh}^{jl}$  (or  $\mathbf{P}_{h-g}^{\delta\gamma}$ , see below) vectors leads to formally the same dipole approximation for MDFF as in the previous MATS algorithm, evaluating Eq. (9). However, in the new algorithm there is no performance penalty in using the complete  $\mathbf{q}$  throughout the whole expression for DDSCS.

Going beyond the dipole approximation would lead to larger matrices  $\mathbb{M}(E)$ , e.g., monopole+dipole model would lead to  $4 \times 4$  matrices and monopole + dipole + quadrupole to  $9 \times 9$  matrices ( $9 = 1 + 3 + 5$ ), etc. They would still be Hermitean, therefore the same approach can be followed.

Löffler et al. have described a similar decomposition of the MDFF [23], which also allows to go beyond the dipole approximation. In Eqs. (10)–(12) of Ref. [23] they define  $\mathbf{g}(\mathbf{q})$ , which could replace  $\mathbf{q}$  in our definition of  $\mathbf{P}_{gh}^{jl}$ , with an appropriate modification of the  $\mathbb{M}(E)$  matrix, see Eq. (14) and compare with Eq. (10) of Löffler et al. After diagonalization, they applied their formalism in real-space approaches to minimize the number of subsequent multislice calculations to propagate the wavefunction after inelastic scattering out of the crystal.

In the expressions above we silently assumed that the Bloch coefficients  $D_h^{(l)}$  and Bloch vector elongations  $\gamma^{(l)}$  will not be strongly dependent on the energy loss. To be more specific, for a core-loss event the Bloch coefficients and elongations are calculated once for a representative energy loss, e.g.,  $E = 710$  eV for the  $L_3$  edge of iron, but their detailed energy dependence within the  $L_3$  edge region between 710 eV and 720 eV is neglected. Then having calculated the  $\mathbf{Q}(\mathbf{a})$  allows us to calculate the DDSCS for an arbitrarily complicated and anisotropic energy dependence of the dipole transitions.

We note that as an insightful secondary output one has an easy access to the partial contributions of individual atoms to the DDSCS, see Eq. (19). While this is common in Yoshioka-equation based multislice approaches, see e.g. [24], this information was not available in MATS due to the analytical summation over unit cells, see Eq. (9).

From the algorithmic point of view, one can speed up the summation by realizing that  $\mathbf{Q}(\mathbf{a})$  depends on  $\mathbf{a}$  only via differences of beams  $\mathbf{h} - \mathbf{g}$  and the elongations  $\gamma^{(l)} - \gamma^{(j)}$ , therefore one can classify the  $\mathbf{P}_{gh}^{jl}$  terms and their corresponding  $\mathbf{q}$  into groups with the same  $\mathbf{s} \equiv \mathbf{h} - \mathbf{g}$  and  $\delta\gamma \equiv \gamma^{(l)} - \gamma^{(j)}$ . By doing so the  $\mathbf{Q}(\mathbf{a})$  can be calculated more efficiently.

Furthermore, in the MS/BW-MATS algorithm [21] the  $\gamma^{(l)}$  are necessarily discretized into integer multiples of  $\frac{2\pi}{t}$ , because discrete Fourier transform of the wavefunction calculated by MS method up to thickness  $t$  cannot contain any shorter Fourier component. In that manuscript it was shown that this discretization does not significantly influence the results, leading to visually indistinguishable diffraction patterns.

Thus it appears tempting to also discretize  $\gamma^{(l)}$ , perhaps on the same grid, allowing to further reduce the number of terms to be summed in calculation of  $\mathbf{Q}(\mathbf{a})$  vectors. However, simply approximating them to the nearest multiple of  $\frac{2\pi}{t}$  is a poor approximation, which differs from the discrete Fourier transform applied to the elastically scattered incoming beam wavefunction. Interestingly, if all  $\gamma^{(j)}$ ,  $\gamma^{(l)}$  factors would be multiples of  $\frac{2\pi}{t}$  then also their linear combinations would be multiples of  $\frac{2\pi}{t}$  and the thickness function, Eq. (8), would be always identically zero, unless the  $\delta\gamma^{(jj')} - \delta\gamma^{(ll')} = 0$ . In summary, if we denote

$$\delta\gamma^{(jj')} - \delta\gamma^{(ll')} = \frac{2\pi n}{t} \quad (24)$$

for an integer  $n$ , then

$$T_{jljl'}(t) \rightarrow \begin{cases} 0 & \text{if } n \neq 0 \\ 1 & \text{if } n = 0 \end{cases} \quad (25)$$

which is a too crude approximation. For example this would not give the characteristic Pendellösung oscillations in the two-beam orientation [25]. The correct way to do that would be to evaluate the outgoing beam wavefunction on a grid, perhaps the same as for the incoming beam wavefunction, and perform a discrete Fourier transform. That would lead to thickness-dependent Fourier components, restoring effects such as Pendellösung. Given the convenient behavior of thickness function, this might be an attractive route for alternative algorithms, perhaps purely multislice-based.

Yet, returning to the main thread, a discretization of  $\gamma^{(l)}$  is a viable path to make the algorithm more efficient. Nevertheless, the



mesh must be finer than multiples of  $\frac{2\pi}{t}$ . In our simulations we chose such a discretization, so that the phase of any discretized exponential term will not be wrong by more than by  $\frac{\pi}{1000}$ . This was tested to provide well-converged calculations and yet speed-up the simulations typically by an order of magnitude, compared to an algorithm without discretization. From the implementation point of view, this grouping is efficiently implemented via associative arrays, which are used to keep track about what combinations of  $\mathbf{h} - \mathbf{g}$  and  $\delta\gamma$  have been already encountered, when constructing the lists of  $\mathbf{P}_{\mathbf{h}-\mathbf{g}}^{\delta\gamma}$ .

We demonstrate the superior convergence properties of the new method on two test examples. The first example is a calculation for an electron probe accelerated by voltage of 200 kV, having a convergence semi-angle of 10 mrad. All aberrations of the electron optics were assumed to be zero. This electron probe passes through a crystal of bcc iron oriented in a three-beam orientation with Bragg spots  $\mathbf{G} = \pm(200)$ , obtained by tilting from the zone axis (001) by approximately  $9.5^\circ$ . This can also be described as a “zone axis” orientation (016). The total thickness of the crystal along the beam direction is 10.5 nm. The orthogonal structure model of bcc-Fe in three-beam orientation is depicted in Fig. 1(a)–(c), having dimensions  $a \times \sqrt{37}a \times \sqrt{37}a$ , where  $a = 2.87$  Å is the lattice parameter of bcc-Fe. Thickness of 10.5 nm is obtained by repeating the structure model 6 times along the  $c$ -axis of the supercell. In the lateral dimensions, the supercell was repeated 18 times along the  $a$  axis and 3 times along the  $b$  axis, reaching  $5.17 \times 5.24$  nm<sup>2</sup> area, which safely contains the beam wavefunction across the whole thickness of the sample, preventing unphysical overlaps with its periodic images.

This example was chosen, because in the 3-beam orientation the dynamical diffraction effects are less pronounced than in low-index zone axis orientation. This is due to a lower number of Bragg spots in diffraction patterns, which typically are concentrated within a so-called systematic row of reflections containing transmitted beam and multiples of  $\mathbf{G} = (200)$ . The basis itself is much larger, consisting of over 200 beams.

The results of the calculations of Fe- $L_3$  edge energy filtered diffraction pattern are shown in Figs. 2 and 3. We show separately the non-magnetic part and the magnetic (EMCD [26]) part of the intensity in the diffraction pattern. These were obtained by setting  $N(E) = 1$  or  $M(E) = 1$  in Eq. (20) or Eq. (22), respectively. The calculations were performed for three different cut-off conditions. At the lowest cut-off  $10^{-4}$  MATS calculation predicts a spurious minimum of intensity in the center of the diffraction pattern, which is an artifact of an unconverged calculation. It is particularly well seen (dashed red curve) in Fig. 3, where intensity profiles for all three convergence criteria are compared for both methods, MATS and the new algorithm, respectively. Tightening the convergence criterion to  $10^{-5}$  makes the minimum more shallow, and it disappears at  $10^{-6}$ . For larger scattering angles the differences are less pronounced. This demonstrates the above-mentioned effect of MATS for the smallest scattering angles. Naturally, for a sufficiently tight convergence criterion, this artifact is not present anymore. Artifacts can also be seen in the magnetic signal, where the least converged calculation shows some sharp features. The two most precise calculations show only minor differences.

Looking at the calculation results of the new algorithm, visually it is very hard to see any differences among the results for all three convergence criteria. That means that converged results are obtained at lower cut-off, which means typically a substantially shorter computing time. Slight differences can only be seen in the intensity profiles, Fig. 3, where the solid red line ( $C_{\text{off}} = 10^{-4}$ ) deviates a tiny bit from the curves extracted at tighter convergence criteria.

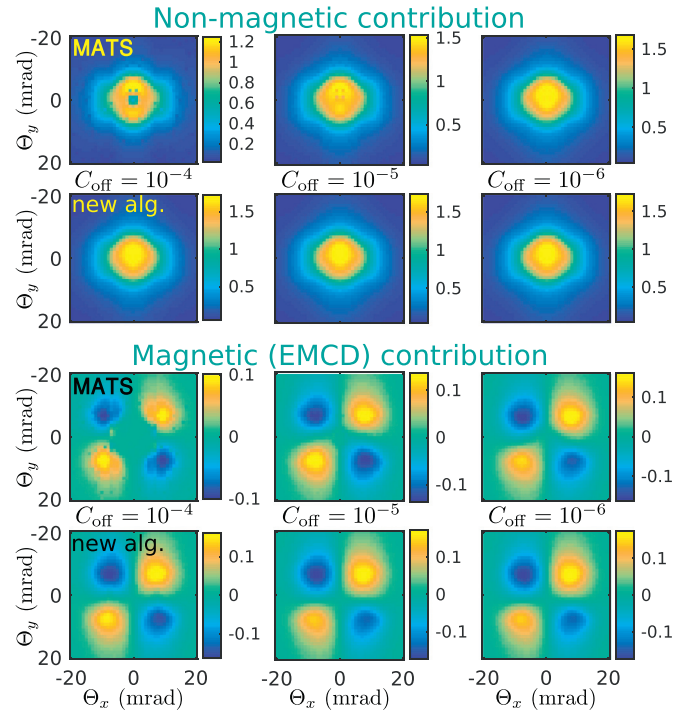


**Fig. 2.** Energy filtered diffraction patterns calculated for  $L_3$  edge of bcc-Fe crystal tilted into systematic row conditions with  $\mathbf{G} = (200)$ . Acceleration voltage is 200 kV, semi-convergence angle 10 mrad. The non-magnetic and magnetic parts of the intensity are shown separately. The intensity scale is in arbitrary units. The method (MATS vs. new algorithm) and the used cut-off condition is indicated inside or next to each panel separately.

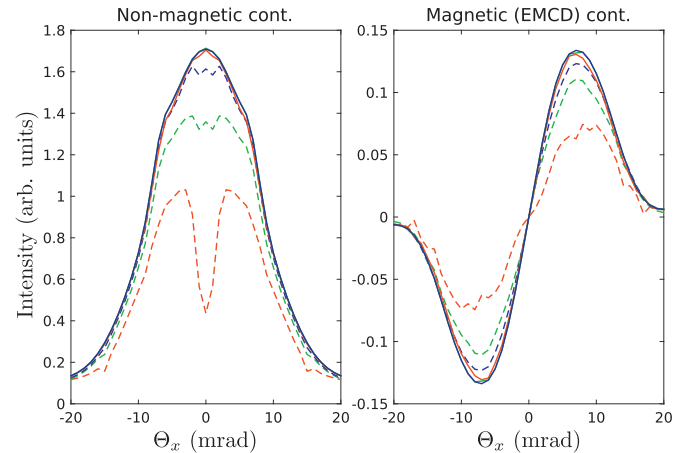


**Fig. 3.** Intensity profiles from diffraction patterns in Fig. 2. Non-magnetic component profiles (left) are shown for  $\Theta_y = 0$ , while magnetic components profiles (right) are at  $\Theta_y = 10$  mrad, passing near the local maxima. Dashed and full lines denote MATS and the new algorithm, respectively. Red, green and blue lines map to the panels of Fig. 2 from left to right, i.e., cut-off conditions  $C_{\text{off}} = 10^{-4}$ ,  $10^{-5}$ ,  $10^{-6}$ , respectively. (For interpretation of the references to color in this figure legend, the reader is referred to the web version of this article.)

Importantly, both methods result in the same diffraction patterns (at least for the highest convergence criterion), including the intensity ranges. Small differences remain between MATS calculation and the results of new algorithm only at the smallest convergence angles, see Fig. 3, better seen in the non-magnetic component of the intensity profile.

Note that at a fixed convergence criterion the two methods do not necessarily give identical results. The reason is that MATS ignores all octuple products of Bloch coefficients (Eq. (2)) that are smaller than a given cut-off. In the new algorithm, some such oc-

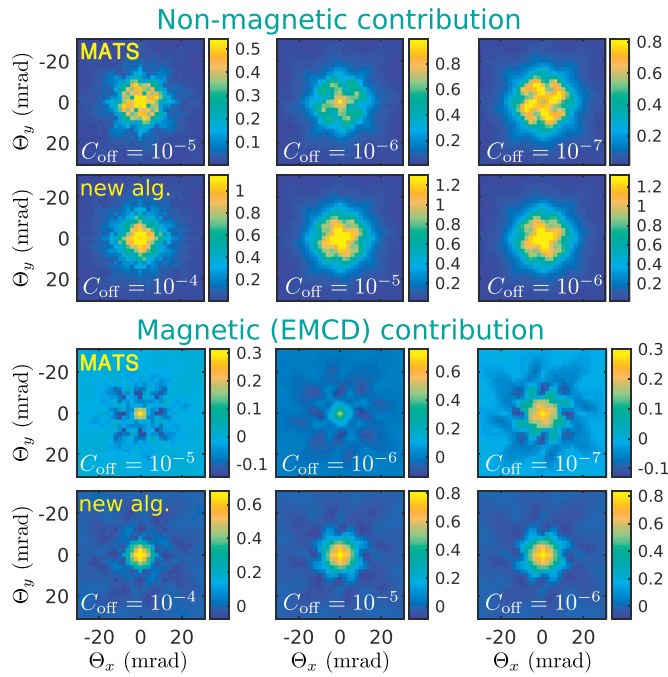


**Fig. 4.** Energy filtered diffraction patterns calculated for  $L_3$  edge of FePt crystal oriented in (001) zone axis orientation. Acceleration voltage is 300 kV, semi-convergence angle 9 mrad, orbital angular momentum of the vortex beam is  $1\hbar$ . The non-magnetic and magnetic parts of the intensity are shown separately. The intensity scale is in arbitrary units. The method (MATS vs. new algorithm) and the used cut-off condition is indicated inside individual panels.

tuple products will enter the summation, because the cut-off is only applied to quadruple products of Bloch coefficients present in Eq. (11). Multiplication of two such quadruple products can easily give a value below the cut-off, see Eqs. (17)–(19).

Apart from the convergent beam calculation discussed here, we have also performed a calculation with a parallel beam (not shown) for the same structure. In this case the diffraction patterns converged very quickly for both methods and the results were well converged already at cut-off  $10^{-4}$ . Thus these results were not very instructive for discussing convergence properties, other than stating that both methods performed well.

The second example represents a more thorough check of the convergence. We have calculated Fe- $L_3$  edge energy filtered diffraction patterns for an electron vortex beam [27] accelerated by voltage of 300 kV, having convergence semi-angle of 9 mrad, and passing through 14.5 nm of FePt crystal, see Fig. 1(d). Such a vortex beam has a full-width at half-maximum of about 2.7 Å. The electron beam is passing through the center of Fe atomic column in a direction parallel to the  $c$ -axis of the FePt unit cell. This represents a zone axis orientation. Moreover the crystal contains a strong scatterer, a heavy element, Pt. Such combination leads to strong dynamical diffraction effects with a large number of beams. The basis size for the Bloch waves part of the calculation was about 460.

The results of calculations are summarized in Figs. 4 and 5. Comparison of MATS with the new method reveals rather large differences at fixed cut-off, which was discussed above. However, while in the previous test example both methods eventually reached the same converged diffraction patterns, here, strikingly, with MATS the absolute convergence is not reached even for a cut-off condition of  $10^{-7}$ , which is already a very expensive calculation. This is highlighted in Fig. 5, which shows non-magnetic and magnetic component intensity profiles through the center of diffraction patterns. Qualitatively the non-magnetic part of the diffraction pattern appears rather similar for the two highest

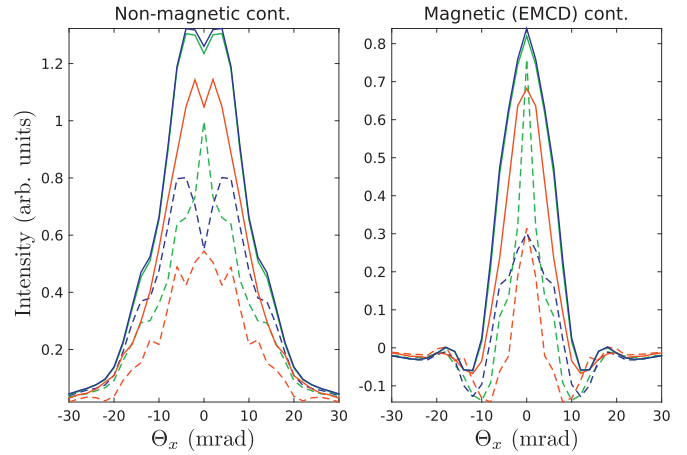


**Fig. 5.** Intensity profiles from diffraction patterns in Fig. 4. Non-magnetic (left) and magnetic (right) components profiles are extracted at  $\Theta_y = 0$  mrad. Dashed and full lines denote MATS and the new algorithm, respectively. Red, green and blue lines map to the panels of Fig. 4 from left to right. (For interpretation of the references to color in this figure legend, the reader is referred to the web version of this article.)

**Table 1**

Computing times for various cut-off conditions. The times represent total time that it took to calculate an energy-filtered diffraction pattern for FePt (like those shown in Fig. 4) on a computer cluster, running 64 CPU cores in parallel.

Method	$10^{-4}$	$10^{-5}$	$10^{-6}$	$10^{-7}$
MATS	1 min	5 min	87 min	2640 min
New alg.	3 min	13 min	90 min	–

convergence criteria, but this is less so in the magnetic part of the diffraction pattern. Contrary to this behavior, the new algorithm shows a clear absolute convergence, which is reached already at cut-off  $10^{-5}$ . The calculation for cut-off  $10^{-6}$  shows in Fig. 4 no visual difference from the one at  $10^{-5}$  and the intensity profiles in Fig. 5 confirm that the absolute differences are negligible. This also means that the new algorithm performs a converged calculation at a dramatically lower computational cost, compared to MATS calculation, see Table 1. On the other hand, we observe that the MATS calculation at the highest cut-off reproduces qualitative features of a converged calculation.

Note that at the same cut-off condition, the new algorithm performs a bit slower than MATS, see Table 1. The speed advantage of the new algorithm originates in a less strict cut-off needed to obtain a fully converged calculation. We remind the reader that the new algorithm performs in its final step a sum over atoms in the sample, Eq. (19), and as such it becomes progressively slower for thicker samples, while MATS is independent of sample thickness due to an analytical sum over atom positions. Therefore, for a sufficiently thick sample in three-beam orientation MATS likely becomes faster. However, in zone axis orientation for sample thicknesses of few tens of nanometers, the new algorithm greatly outperforms MATS.

In summary, the new algorithm performs consistently well in all of the tested scenarios, reaching absolute convergence at acceptable computing costs. In some situations with strong dynamical diffraction effects this new algorithm, to which we will refer in the future as MATS.v2, performs significantly faster.

## Acknowledgments

We acknowledge Swedish Research Council, Göran Gustafsson's Foundation and STINT for financial support. The computations were performed on resources provided by the Swedish National Infrastructure for Computing (SNIC) at NSC center.

## References

- [1] J.M. Cowley, A.F. Moodie, *Acta Cryst.* 10 (1957) 609.
- [2] K. Ishizuka, N. Uyeda, *Acta Cryst. A* 33 (1977) 740–749.
- [3] E.J. Kirkland, *Advanced Computing in Electron Microscopy*, 2nd edition, Springer, 2010.
- [4] M. Inokuti, *Rev. Mod. Phys.* 43 (1971) 297–347.
- [5] A.J.F. Metherell, in: *Electron Microscopy in Materials Science II*, CEC, Luxembourg, 1975, p. 397.
- [6] Y. Kainuma, *Acta Cryst. A* 8 (1955) 24.
- [7] C.J. Rossouw, V.W. Maslen, *Phil. Mag. A* 49 (1984) 743–757.
- [8] H. Kohl, H. Rose, *Adv. Electron. Electron Opt.* 65 (1985) 173–226.
- [9] D.K. Saldin, *Phil. Mag. B* 56 (1987) 515–525.
- [10] A. Weickenmeier, H. Kohl, *Phil. Mag. B* 60 (1989) 467.
- [11] M. Nelhiebel, P.-H. Louf, P. Schattschneider, P. Blaha, K. Schwarz, B. Jouffrey, *Phys. Rev. B* 59 (1999) 12807.
- [12] S.D. Findlay, L.J. Allen, M.P. Oxley, C.J. Rossouw, *Ultramicroscopy* 96 (2003) 65–81.
- [13] C. Dwyer, *Ultramicroscopy* 104 (2005) 141.
- [14] M.P. Oxley, M.D. Kapetanakis, M.P. Prange, M. Varela, S.J. Pennycook, S.T. Pantelides, *Microsc. Microanal.* 20 (2014) 784.
- [15] L.J. Allen, A.J. D'Alfonso, S.D. Findlay, *Ultramicroscopy* Vol. 151 (2015) 11–22.
- [16] P. Schattschneider, M. Nelhiebel, B. Jouffrey, *Phys. Rev. B* 59 (1999) 10959.
- [17] J. Verbeeck, P. Schattschneider, A. Rosenauer, *Ultramicroscopy* 109 (2009) 350.
- [18] J. Ruzs, S. Muto, K. Tatsumi, *Ultramicroscopy* 125 (2013) 81–88.
- [19] P. Schattschneider, M. Nelhiebel, M. Schenner, W. Grogger, F. Hoffer, *J. Microsc.* 183 (1996) 18.
- [20] D. Song, J. Ruzs, J. Cai, J. Zhu, *Ultramicroscopy* 169 (2016) 44.
- [21] J. Ruzs, S. Bhowmick, M. Eriksson, N. Karlsson, *Phys. Rev. B* 89 (2014) 134428.
- [22] J. Ruzs, S. Rubino, O. Eriksson, P.M. Oppeneer, K. Leifer, *Phys. Rev. B* 84 (2011) 064444.
- [23] S. Löffler, V. Motsch, P. Schattschneider, *Ultramicroscopy* 131 (2013) 39.
- [24] B.D. Forbes, L. Houben, J. Mayer, R.E. Dunin-Borkowski, L.J. Allen, *Ultramicroscopy* 147 (2014) 98.
- [25] A. Howie, M.J. Whelan, *Proc. R. Soc. A* 263 (1961) 217.
- [26] P. Schattschneider, S. Rubino, C. Hébert, J. Ruzs, J. Kuneš, P. Novák, E. Carlino, M. Fabrizio, G. Panaccione, G. Rossi, *Nature* 441 (2006) 486.
- [27] K.Y. Bliokh, Y.P. Bliokh, S. Savelev, F. Nori, *Phys. Rev. Lett.* 99 (2007) 190404.